Published in IET Control Theory and Applications
Received on 7th November 2007
Revised on 27th February 2008
doi: 10.1049/iet-cta:20070415

ISSN 1751-8644

H_2 and H_∞ robust autopilot synthesis for longitudinal flight of a special unmanned aerial vehicle: a comparative study

F. Santoso   M. Liu   G. Egan

Department of Electrical and Computer Systems Engineering, Monash University, VIC 3800, Melbourne, Australia
E-mail: fendy_santoso@yahoo.co.uk

Abstract: The aim of this paper is to investigate the feasibility of robust H_2 and H_∞ autopilots to the longitudinal flight motions of a flying wing unmanned aerial vehicle (UAV), P15035, developed by Monash Aerobotics Research Group. The challenge associated with this UAV is related to the fact that all motions are controlled by two independently actuated ailerons, namely elevons, together with its throttle. The scope of this research is nonetheless limited only for elevon control based on the trimmed linear longitudinal flight modes obtained experimentally from the previous study, while the throttle is a constant. Since the real environment is subject to modelling uncertainties and variations, robust H_2 and H_∞ control systems are designed to withstand such uncertainties and variations. Simulations indicate that the control systems designed poss acceptable performances both in time and frequency domain, with reasonable settling time and overshoots while maintaining reasonably robust stability. It further shows that robust H_∞ autopilot has demonstrated superior time domain performances compared with the H_2 counterpart.

1 Introduction

The ultimate design that the unmanned aerial vehicle (UAV) engineers wish to achieve is to provide autonomous systems from taking off, cruising to landing. In order to achieve this goal, feedback control systems must satisfy both robust stability and robust performances for a particular dynamic system. The main reason to employ robust control is in fact to overcome the existing disturbances, for example, atmospheric turbulences, noise, as well as uncertainty in modelling.

Our research aircraft P15035 (Fig. 1) belongs to the class of aircraft called flying wings and is known colloquially as a 'plank' having an unswept constant chord (width) wing of low aspect (length to width) ratio and no rudder or elevator in the sense of a more conventional aircraft (see Table 1 for technical details). A number of advantages have been claimed for flying wings including reduced parasitic drag due to the absence of an extended tail and associated elevator and rudder control surfaces. In our case we chose a plank as it is very rugged, of compact construction and has, at least for human pilots, very benign flight behaviour and wide airspeed range; autopilot design and tuning is a little more challenging.

The P15035 has two elevon control surfaces which combine the functions of elevators and ailerons. Pitch is controlled by the average deflection of the elevons and roll by the difference. While there is a vertical stabiliser it has no attached rudder and so yaw control is indirect through roll. The aircraft does not have the usually long moment arm provided by elevators; it must rely upon a slight upsweep in the rear of the airfoil to maintain a positive pitching moment to overcome the moments introduced by a forward centre of gravity this being essential to maintain stability. Partially as a consequence of this there is an increased coupling between throttle and pitch. We have assumed constant cruise throttle setting in this paper.

To further complicate matters we fly at relatively at low Reynolds number (<250 K) regimes, which means turbulent

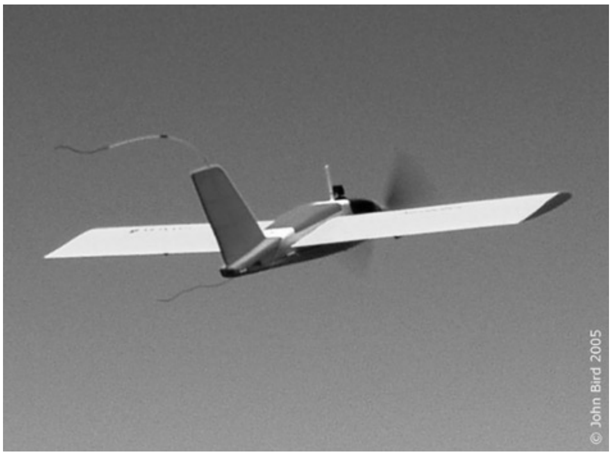

Figure 1 *P15035 aircraft*

(Reproduced with the permission of J. Bird, a member of Monash Aerobotics Research Group)

flow and laminar separation across wing surface. Air turbulence is also of concern due to the size of the aircraft, see [1–3] for more comprehensive explanations. As a result, the aircraft dynamics are obviously nonlinear and at times varying. In relation to this matter, interested readers are suggested to refer to [1–3] and also [4–7]. More comprehensive information regarding this small UAV controls is given in Section 2.

Our preliminary work in identification for the aircraft has been published in [1], with extension to this work is found in [2, 3]. Relevant control theory related to system identification could be found in [8–11]. Topics correspond to robust control synthesis may be found in [14–16]. Extended theory about dynamic systems may be found in [17–19]. In addition, we have at our disposal a large repository of flight logs for our aircraft. It contains the complete dynamics record of flight data [20].

In the model-based control system, especially the observer-based ones, there always exist uncertainty and modelling errors. Since the identified model is used to design the real-time control systems, consequently, this will certainly degrade the robustness of the closed-loop control system. In worst case, the design results may not work practically due to the lack of robustness. As a result, robust control systems have been widely developed. Yet another advantage

Table 1 Specifications of Aircraft P15035

span	150 cm	motor	electric
chord	35 cm	duration	40–60 min
length	106 cm	speed	33–150 km/h
control surface	elevon	battery	28 × GP3300NiMh
weight	2.9–4.6 kg	autopilot	MP2028

of employing robust control is when it comes to the simplicity in designing for multivariable systems.

In this study, we consider designing robust autopilot using H_2 and H_∞ synthesis. It is well known that H_2 synthesis is equivalent to linear quadratic gaussian (LQG) optimal control design. Regarding to its preliminary design results, interested readers are suggested to refer to [2, 3]. Some recent works on robust control may be found in [21–23]. The term 'synthesis' refers to theoretical development, precise and unambiguous, whose aim is mainly pedagogical [16].

Furthermore, the availability of robust control toolbox in MatLab has simplified the composition process. The offline computation algorithm also has made the composition process more computationally intensive rather than the real-time control loops computed in flight, where we have electrical and computational power limitations [3].

The organisation of this paper is as follows. First, Section 1 depicts some issues related to background, organisation and motivation of this research. In Section 2, the open-loop mathematical model of elevon-average-to-altitude is introduced together with the study of its time domain characteristics. Sections 3 deals with some robustness issues. Subsequently, in Sections 4–6, robust autopilot H_2 and H_∞ will be synthesised together with the study of both their frequency domain as well as time domain performances. Lastly, conclusions will be drawn in Section 7.

2 Open-loop mathematical model

Generating a comprehensive nonlinear model for the aircraft is usually impractical. Instead, a more realistic approach is to develop a set of linearised models valid for different dynamic ranges. Longitudinal and lateral models for conventional larger aircraft are well understood [8–11]. It is assumed that the longitudinal dynamics is to be uncoupled from its lateral motions. Pitch is controlled by the average deflection of the elevons, meanwhile, roll is controlled by the elevon deflections in an attempt to control yaw and to minimise the adverse drag.

The longitudinal and lateral directional models for the P15035 have been obtained using system identification techniques [9–11] based on real flight data and were initially reported in [1]. Consider the trimmed model in which the throttle is constant, two controllable inputs of the model are right elevon, left elevon and three outputs are given by output state vector $[p, q, r]^T$, representing rates of pitch, roll and yaw vectors, respectively. Hence, the linear trimmed model of our flying wing UAV can be depicted as follows [1]

$$\begin{bmatrix} p \\ q \\ r \end{bmatrix} = \begin{bmatrix} G_{11} & G_{12} \\ G_{21} & G_{22} \\ G_{31} & G_{32} \end{bmatrix} \begin{bmatrix} \delta_l \\ \delta_r \end{bmatrix} \tag{1}$$

where δ_l and δ_r represent left and right elevons, respectively, (degree) and G_{ij} are the corresponding transfer functions.

IET Control Theory Appl., 2008, Vol. 2, No. 7, pp. 583–594
doi: 10.1049/iet-cta:20070415

Due to the symmetrical properties of the aircraft about its x–z plane, consequently, the effects of left and right elevons are identical to the pitch but opposite to the roll and yaw, therefore we have that $G_{11} = G_{12}$, $G_{21} = -G_{22}$, $G_{31} = -G_{32}$. By denoting $G_P = G_{11}$, $G_R = G_{21}$ and $G_Y = G_{31}$, it eventually leads to the following equation [1]

$$\begin{bmatrix} p \\ q \\ r \end{bmatrix} = \begin{bmatrix} G_P & 0 \\ 0 & G_R \\ 0 & G_Y \end{bmatrix} \begin{bmatrix} \delta_A \\ \delta_D \end{bmatrix} \tag{2}$$

where δ_A and δ_D are associated with elevon average and elevon difference, respectively, given by $\delta_A = \delta_l + \delta_r$ (or $\delta_A = (\delta_l + \delta_r)/2$, if G_p becomes $2G_p$) and $\delta_D = \delta_l - \delta_r$. From (2), pitch is independently controlled by elevon average deflection δ_A, corresponding to the elevators of a conventional aircraft, and roll and yaw are both driven by elevon difference δ_D, corresponding to the aileron and rudder for a conventional aircraft. Consequently, no decoupling can be made between yaw and roll due to special configuration of the aircraft.

For trimmed flight with a constant engine thrust the P15035's longitudinal discrete time transfers function from the elevon average deflection δ_A to the pitch angle θ (which is the integral of pitch rate) with a sampling frequency of 5 Hz is obtained as

$$\left.\frac{\theta(z)}{\delta(z)}\right|_{5\,\text{Hz}} = \frac{-0.13065z^2(z+0.0091)}{(z-0.9115)(z-0.9785)(z^2+0.2267z+0.3763)} \tag{3}$$

in which its complex conjugate poles are given by:$z = -0.1134 \pm 0.6029i$.

Converted to s domain, it becomes

$$\frac{\theta(s)}{\delta_A(s)} = \frac{-0.2954(s+6.693)(s^2+11.7s+91.49)}{(s+0.4633)(s+0.1087)(s^2+4.887s+83.12)} \tag{4}$$

with a pair of complex conjugate pole given by: $s = -2.4435 \pm 8.7835i$.

It is well known (e.g. [4, 5, 7, 24]) that the typical longitudinal dynamics of a traditional aircraft (elevator to pitch) with a constant engine thrust can be expressed as:

$$\frac{\theta(s)}{\delta(s)} = \frac{k_\theta(s+1/T_{\theta_1})(s+1/T_{\theta_2})}{(s^2+2\varsigma_p\omega_p s+\omega_p^2)(s^2+2\varsigma_s\omega_s s+\omega_s^2)} \tag{5}$$

In (5) δ is now the elevator angle [instead of the elevon average in (4)], k_θ the high-frequency gain, $\Delta s_p = s^2 + 2\varsigma_p\omega_p s + \omega_p^2$ the so-called phugoid mode, and $\Delta s_s = s^2 + 2\varsigma_s\omega_s s + \omega_s^2$ the short period mode, ς_p and ς_s the damping factors and ω_p and ω_s the undamped natural frequency of the two modes, respectively. Typically, the phugoid mode is overdamped with a relatively large time constant and the short period mode represents underdamped oscillations. The overall pitch step response is a combination of a slow exponential function and quickly decaying high-frequency oscillations.

Comparing (4) with (5), it can be seen that the longitudinal model (4) has an over damped phugoid model given by $\Delta s_p = (s+0.4633)(s+0.1087)$ with a dominant large time constant of $\tau = 10$ s. Its short period model is given by $\Delta s_s = s^2 + 4.887s + 83.12$ with a damping ratio of 0.268 and a natural frequency of 9.12 rad/s. The settling time is small, being in the order of 1 s. The impulse responses are plotted in Fig. 2.

Since in this research, we are considering the altitude-holding control we need to determine the elevon-to-altitude transfer function for autopilot designs. Given the pitch-to-altitude transfer function in z domain with a sampling frequency of 5 Hz as

$$\frac{h(z)}{\theta(z)} = \frac{0.05456z}{z-0.9969} \tag{6}$$

where h is the altitude of the aircraft in metres obtained from flight data modelling. We finally obtain the following elevon-to-altitude transfer function in s domain as:

$$\frac{h(s)}{\delta_A(s)} = \frac{-0.011659(s^2+11.88s+42.46)(s^2+9.723s+99.83)}{(s+0.4633)(s+0.1087)(s+0.01552)(s^2+4.887s+83.12)} \tag{7}$$

From (7) the linearised model of the longitudinal dynamics can be expressed in state space equations given by

$$\begin{aligned} \dot{x} &= Ax + Bu \\ y &= Cx + Du \end{aligned} \tag{8}$$

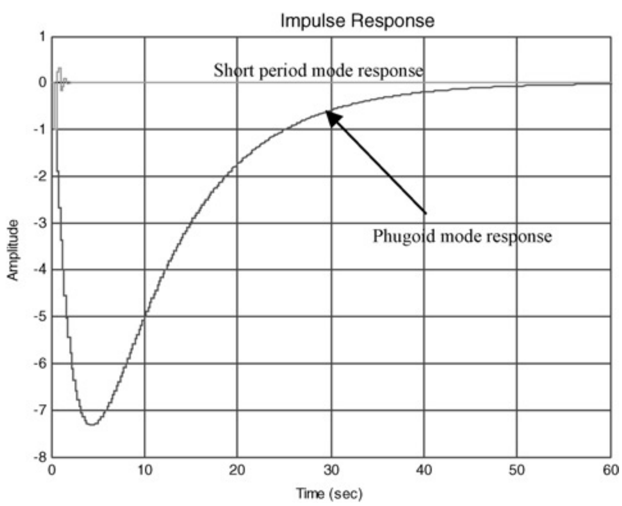

Figure 2 *Impulse pitch amplitude responses in degrees for phugoid and short period modes of UAV P15035*

doi: 10.1049/iet-cta:20070415

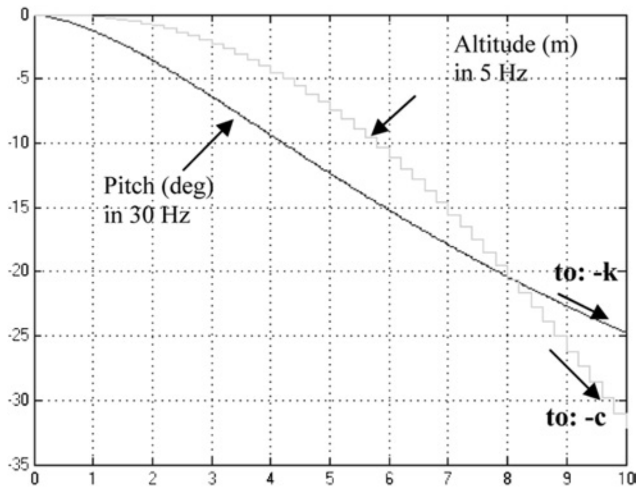

Figure 3 *Open-loop time domain responses of elevon-average-to-pitch and elevon-average-to-altitude*

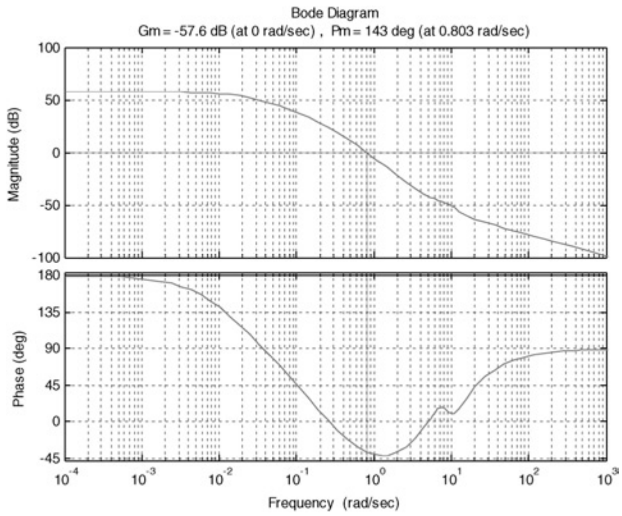

Figure 4 *Frequency response of the open-loop elevon-average-to-altitude*

in which, $u = \delta_A$, $y = h$ and x is the state vector defined accordingly:

$$A = \begin{bmatrix} -5.4740 & -86.0500 & -49.120 & -4.9270 & -0.0650 \\ 1 & 0 & ,0 & 0 & 0 \\ 0 & 1 & 0 & 0 & 0 \\ 0 & 0 & 1 & 0 & 0 \\ 0 & 0 & 0 & 1 & 0 \end{bmatrix},$$

$$B = [1\ 0\ 0\ 0\ 0]^T,$$
$$C = [-0.0117 - 0.2519 - 3.0060 - 18.640 - 49.4200],$$
$$D = [0]$$

The open-loop impulse responses of elevon-average-to-pitch as well as elevon-average-to-altitude are given by Fig. 3. It turns out that the final dc values of both pitch and altitude with respect to a unit step input are negative constants, that is, $-k$ and $-c$, where $k \neq c$, as we expect in real flight. The reason to employ different sampling rate is due to the fact that altitude changes are very slow compared with the airframe rates. While we could run all of the loops at a high rate there is usually a computational throughput limit in the control processor which forces us to run only the primary attitude loops at the high rate.

Meanwhile, the open-loop altitude frequency response is depicted in Fig. 4. The negative open-loop gain margin indicates that the open-loop rigid body model experiences lack of robust stability and performances.

3 Uncertainty and robustness issues

This section deals with synthesis and analysis of robust autopilot to the longitudinal flight motion of the UAV, P15035. Some robustness issues will be depicted first, before subsequently followed by problem its formulations including performances and robustness objectives and also the design procedures.

3.1 Signal and system norms

As a standard measure of how big the signal $x(t)$ under sinusoidal excitation, the definition of a particular system gain can be represented using different norms, that is, [16]:

- The L_2-norm represents the total energy associated with the signal, given by:

$$\|x\|_2 = \sqrt{\int_0^\infty x^2(t)\,dt}$$

- The L_∞-norm is given by:

$$\|x\|_\infty = \sup_t |x(t)|$$

It is the magnitude of the peak value of the Bode diagram.

Subsequently, in this section we will be depicting two important system norms, that is,

- For a stable single input single output (SISO) linear system with transfer function G(s), the H_2-norm is defined as:

$$\|G\|_2 = \left(\frac{1}{2\pi}\int_{-\infty}^{\infty} |G(j\omega)|^2 d\omega\right)^{1/2}$$

- In addition to the H_2-norm, H_∞-norm provides a measure of the worst case system gain. For a stable SISO linear system

doi: 10.1049/iet-cta:20070415

with transfer function G(s). The H_∞-norm is given by:

$$\|G\|_\infty = \sup_\omega |G(j\omega)|$$

3.2 Classical stability margin

Classical stability margin can be represented using two parameters, that is, gain margin (GM) and phase margin (PM). GM can be defined as the factor by which the gain can be increased before the system is unstable. It also becomes the standard measure of the system's relative stability. The GM of a stable system has to be positive. This is also desirable from the point of view of robustness. Another parameter associated with relative stability is called PM, which indicates the additional phase lag that will make the system marginally stable.

3.3 Robust stability margin

For stability analysis, the command reference signal is not required; it can be set to zero. Let $\Delta(j\omega)$ be the maximum uncertainty that can be tolerated by the closed-loop control system while still maintaining its stability, and $T_o(j\omega) = L_o/(1 + L_o)$ be the complementary sensitivity function in which L_o is the open-loop gain (as shown in Fig. 5), according to the small gain theorem the stability of closed-loop system can be guaranteed if $\|\Delta(j\omega)T_o(j\omega)\|_\infty < 1$. It can be rewritten as:

$$|\Delta(j\omega)| < \frac{1}{|T_o(j\omega)|}, \quad \forall\omega \tag{9}$$

Suppose the closed-loop transfer function varies from $T(s)$ to $T(s) + \Delta T(s)$ due to the variation of plant parameters from $G(s)$ to being $G(s) + \Delta G(s)$, the sensitivity function $S(s)$, defined as the ratio of fractional changes in the closed-loop system to the fractional change in the open-loop system, given as:

$$S(s) = \lim_{|\Delta G(s) \to 0|} \frac{\Delta T/T}{\Delta G/G} = \frac{1}{1 + GK} \tag{10}$$

It is now obvious that in order to retain good performance and disturbance rejection $|S_o|$ has to be small. On the other hand, for the sake of stability robustness and noise suppression, the magnitude of the nominal complementary

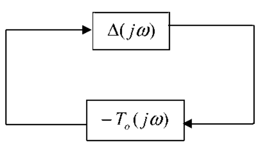

Figure 5 *Robust stability represented in collapse block diagram*

(The negative sign indicates negative feedback applied under zero initial condition)

sensitivity function $|T_o|$ has to be small as well, particularly at higher frequency.

However, due to the relation $T(s) + S(s) = 1$, it is not possible to keep both sensitivity and the complementary function small at the same instance due to the well-known 'water bed effect'. What is achievable instead is to make a trade-off between those two objectives. Mathematically, Bode's sensitivity integral, for a stable system which has no right-half plane zeros, states that:

$$\int_0^\infty \log_{10} |S(j\omega)| \mathrm{d}\omega = 0 \tag{11}$$

Equation (11) indicates that as $|S_o|$ is pushed down on one particular frequency, it will pop up somewhere else in other frequency ranges. In particular, $|S(j\omega)|$ and $|T(j\omega)|$ cannot be <50% at the same frequency [16]. As a common practice, for low frequency around the design bandwidth, denoted by $[0, \omega_b]$, sensitivity is kept to be small, while for the remaining bandwidth, given by $[\omega_b, \infty]$, the complementary sensitivity function is set to be small. The reason for that is due to a good compromise of performance and robustness at this designated frequency region [12–16].

3.4 Robust autopilot problem formulations

We bring our SISO system originally into its equivalent multi input multi output (MIMO) model formulation, which is indeed a more realistic problem formulation. The plant in Fig. 6 can be represented in the following extended state space diagram in 14 as follows

$$\begin{aligned} \dot{x} &= Ax + B_1 w + B_2 u \\ z &= C_1 x + D_{11} w + D_{12} u \\ y &= C_2 x + D_{21} w + D_{22} u \end{aligned} \tag{12}$$

where z is the regulated outputs, that is, the signal we are interested in controlling (in this research: altitude and its control signal), meanwhile, y is signals that are measured and fed back, see (25), become the input of controller. Also, w, u and x correspond to the existing disturbances, input elevon average, and states of the system, respectively. The state space equations in (12) can be expressed in the

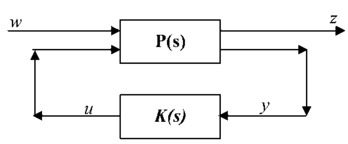

Figure 6 *Two-port block diagram (as a standard problem formulation in robust control) and s = (jω)*

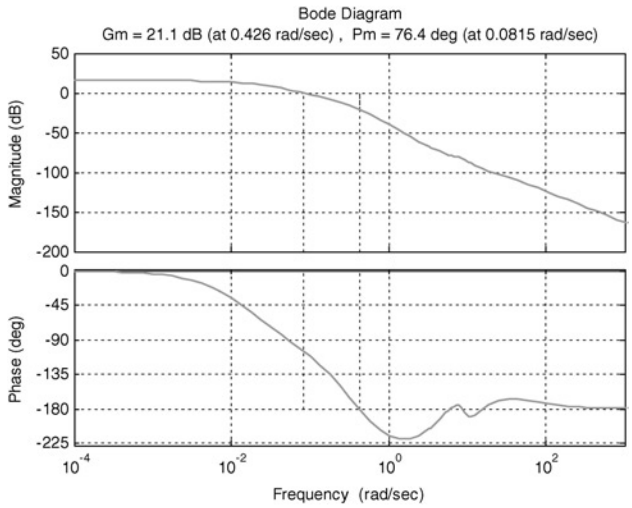

Figure 7 *Open-loop transfer function of H_2 system*

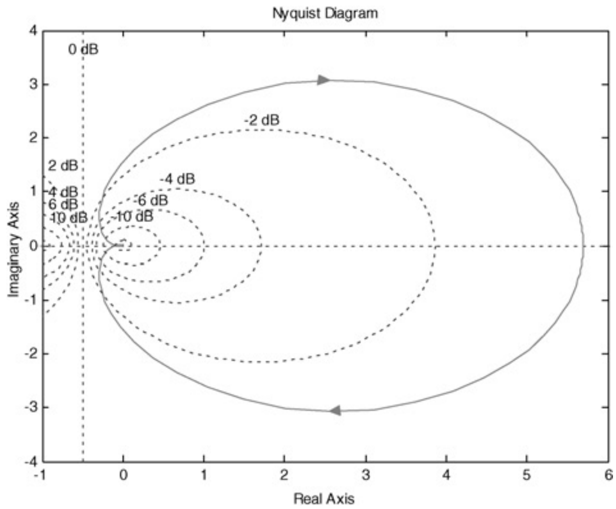

Figure 8 *Nyquist plot for H_2 system*

extended matrix $P(s)$ as follows:

$$P(s) = \left[\begin{array}{c|c:c} A & B_1 & B_2 \\ \hline C_1 & D_{11} & D_{12} \\ \hdashline C_2 & D_{21} & D_{22} \end{array}\right] \tag{13}$$

Robust H_2 control $K(s)$ stabilises the plant and has the same number of states as its open-loop plant $P(s)$. As distinct from H_∞ control, H_2 optimal cost is defined as $\gamma = \left\| T_{yu} \right\|_2$ [25]. Moreover, the resulting robust H_2 control law is given as: $u_2 = K(s)Y(s)$.

4 Robust H_2 design

The optimal solution in H_2 synthesis is obtained by solving two Ricatti equations. The resulting Bode diagram and Nyquist plot of the compensated open-loop transfer function of $G(s)K(s)$ using H_2 is given in Fig. 7, in which its GM and PM for the compensated system are $\text{GM} = 21.1356$ dB and $\text{PM} = 76.3742°$, respectively.

Since both GM and PM expressed in decibels (see Bode diagram in Fig. 7 and Nyquist plot in Fig. 8) are positive, the closed-loop system is definitely stable. Fig. 9 clearly depicts the water bed effect of H_2 system. It is also

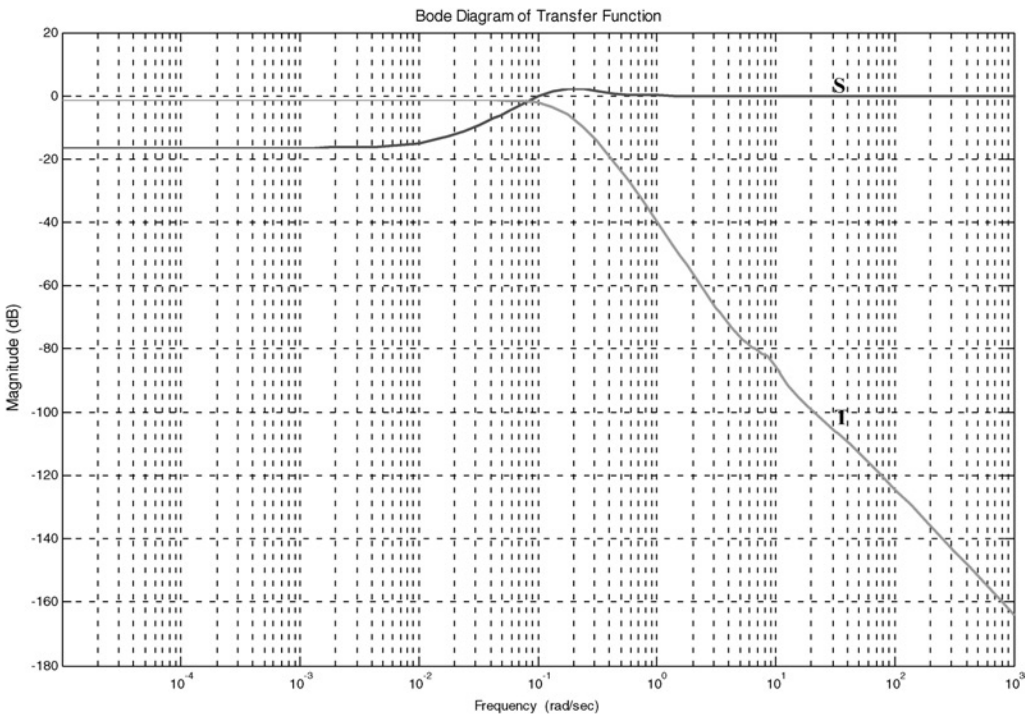

Figure 9 *Sensitivity against complementary sensitivity function for H_2 system*

doi: 10.1049/iet-cta:20070415

Table 2 H_2 autopilot design result

Eigen values	Damping	Frequency
−0.1314	1.000	0.131
−0.123 + 0.103*i*	0.765	0.161
−0.123 − 0.103*i*	0.765	0.161
−0.4581	1.000	0.458
−0.4667	1.000	0.467
−2.443 + 8.7835*i*	0.268	9.120
−2.443 − 8.7835*i*	0.268	9.120
−28.5	1.000	28.5

apparent that for $|L_o| \ll 1$, $|L_o| \simeq |T_o|$, meanwhile for $|L_o| \gg 1$, $L_o \simeq 1/|S_o|$.

The resulting H_2 autopilots should have the same number of states as the transfer function of elevon-average-to-altitude. However, there is a pair of common complex conjugate poles and zeroes given by: $-2.443 \pm 8.7835i$ that can cancel each other. As a result, in terms of pole/zero/gain, the resulting H_∞ compensator is obtained

$$K(s) = \frac{-0.54884(s+0.463)(s+0.1166)}{(s+28.53)(s^2+0.7145s+0.1386)} \tag{14}$$

The resulting closed-loop eigen values, damping factor as well as undamped natural frequency are given in Table 2.

5 Robust H_∞ problem set up

As opposed to time domain LQG control, H_∞ is a frequency-domain-based linear quadratic optimal control, developed in response to address the issue related to the modelling errors and uncertainty [18]. Interested readers may refer to [12–14, 25] and also to [15, 16, 21–23] for further studies. It is in fact a powerful frequency domain optimisation technique to design robust control systems. The name H_∞ refers to the space of stable and proper transfer function, that is, the degree of the denominator is always greater or equals to the degree of the numerator at the same time strictly maintain all poles on the left-hand side of s plane.

As previously defined, the ∞-norm of a transfer function is simply the peak of the Bode magnitude diagram of a transfer function and is defined as:

$$\|G\|_\infty = \sup|G(j\omega)| \tag{15}$$

The objective here is to minimise the ∞-norm of the transfer function, which in turn, minimise the peak of the Bode magnitude plot, in order to enhance robust stability margin of the systems.

Consider the two-port block diagram in Fig. 6, the standard H_∞ problem is to work out an internally stabilising controller, $K(s)$ for the plant $P(s)$, such that the ∞-norm of the closed-loop transfer function, T_{zw}, is below a give positive scalar level, γ.

Mathematically, it can be formulated using the following equations

$$\min_{K(s)\text{stabilising}} \|T_{zw}\|_\infty, \quad \text{find}_{K(s)\text{stabilising}} \|T_{zw}\|_\infty \le \gamma \tag{16}$$

in which, γ is a positive definite scalar. By employing the search algorithm, γ is iterated until the optimal value is reached. Practically, this design approach is to make a delicate balance act of trade-offs [25].

It should be pointed out that there is a common thread between H_∞ and LQG autopilot since both of them employ a state estimator and feed back the estimated states. Ricatti equation is also applied to compute both controller and estimator gains. The difference is however when it comes to the coefficients of Ricatti equations and the fact that some extra terms are introduced in H_∞ state estimator [25].

5.1 H_∞ Problem solutions

The theoretical development of H_∞ synthesis mainly refers to [25]. In the sense of LQG, optimal feedback regulator is given as:

$$u = -k_c\hat{x} \tag{17}$$

The state estimator is then given by

$$\dot{\hat{x}} = A\hat{x} + B_2u + B_1\hat{w} + Z_\infty k_e(y - \hat{y}) \tag{18}$$

in which $\hat{w} = \gamma^{-2}B_1'X_\infty\hat{x}$ and $\hat{y} = C_2\hat{x} + \gamma^{-2}D_{21}B_1'X_\infty\hat{x}$.

The robust compensator can be calculated using the following equations

$$K(s) = \left[\begin{array}{ll} A - B_2k_c - Z_\infty k_e C_2 + \gamma^{-2} & \\ \quad (B_1B_1' - Z_\infty k_e D_{21}B_1')X_\infty & Z_\infty k_e \\ \quad -k_c & 0 \end{array}\right] \tag{19}$$

where,

$$\begin{aligned} k_c &= \tilde{D}_{12}(B_2'X_\infty + D_{12}'C_1) \\ \tilde{D}_{12} &= (D_{12}'D_{12})^{-1} \\ k_e &= (Y_\infty C_2' + B_1D_{12}')\tilde{D}_{21} \\ \tilde{D}_{21} &= (D_{21}'D_{21})^{-1} \end{aligned}$$

doi: 10.1049/iet-cta:20070415

and

$$Z_\infty = (I - \gamma^{-2}Y_\infty X_\infty)^{-1}$$

Moreover, X_∞ and Y_∞ are the solutions of Ricatti equations obtained as follows

$$X_\infty = \mathrm{Ric}\begin{bmatrix} A - B_2\tilde{D}_{12}D'_{12}C_1 & \gamma^{-2}B_1B'_1 - B_2\tilde{D}_{12}B'_2 \\ -\tilde{C}'_1\tilde{C}_1 & -(A - B_2\tilde{D}_{12}D'_{12}C_1)' \end{bmatrix} \tag{20}$$

$$Y_\infty = \mathrm{Ric}\begin{bmatrix} (A - B_1D'_{21}\tilde{D}_{21}C_2)' & \gamma^{-2}C'_1C_1 - C'_2\tilde{D}_{21}C_2 \\ -\tilde{B}_1\tilde{B}'_1 & -(A - B_1D'_{21}\tilde{D}_{21}C_2) \end{bmatrix}$$

in which $\tilde{C}_1 = (I - D_{12}\tilde{D}_{12}D'_{12})C_1$ and $\tilde{B}_1 = B_1\ (I - D'_{21}\tilde{D}_{21}D_{21})$ Finally, the resulting closed-loop system is depicted in the following extended state space equations:

$$\begin{bmatrix} \dot{x} \\ \dot{\hat{x}} \end{bmatrix} = \begin{bmatrix} A & -B_2k_c \\ Z_\infty k_e C_2 & \begin{matrix} A - B_2k_c + \gamma^{-2}B_1B'_1X_\infty \\ -Z_\infty k_e(C_2 + \gamma^{-2}D_{21}B'_1X_\infty) \end{matrix} \end{bmatrix} \times \begin{bmatrix} x \\ \hat{x} \end{bmatrix} + \begin{bmatrix} B_1 \\ Z_\infty k_e D_{21} \end{bmatrix} w \tag{21}$$

The output equation is then given as follows:

$$\begin{bmatrix} z \\ y \end{bmatrix} = \begin{bmatrix} C_1 & -D_{12}k_c \\ C_2 & 0 \end{bmatrix}\begin{bmatrix} x \\ \hat{x} \end{bmatrix} + \begin{bmatrix} 0 \\ D_{21} \end{bmatrix} w \tag{22}$$

A stabilising compensator will exist if and if only

$$\rho(X_\infty Y_\infty) < \gamma^2 \tag{23}$$

where $\rho(A)$ is the spectral radius of (A), $\rho(A) = \lambda_{\max}(A)$. In fact, for every value of γ, there are two Ricatti equations that must be solved.

5.2 Robust H_∞ autopilot – problem formulations

First, the two-port input, which corresponds to actual disturbances or to un-modelled dynamics of the systems are introduced as

$$w = [d_1 \quad d_2 \quad d_3 \quad d_4 \quad n]^{\mathrm{T}} \tag{24}$$

in which d_1 corresponds to input elevon average disturbance, while d_3 and d_2 denote pitch and pitch rate disturbances, respectively. Also, d_4 is the altitude noise due to input elevon average and n is the existing measurement noise in flight.

The performance objective we would like to achieve here is to synthesise a stabilising H_∞ autopilot that can achieve the closed-loop performance objectives, for example, the desired (minimum) sensitivity function bellow 0 dB or about one over a particular frequency range.

By incorporating the newly introduced terms in (24) into state equation obtained in (13), we finally arrive at the extended state space equation as follows

$$\begin{aligned} \dot{x}_1 &= -5.4740x_1 - 86.05x_2 - 49.12x_3 - 4.927x_4 \\ &\quad - 0.065x_5 + u + d_1 \end{aligned} \tag{25}$$

$$\dot{x}_2 = x_1$$
$$\dot{x}_3 = x_2$$
$$\dot{x}_4 = x_3$$
$$\dot{x}_5 = x_4 + d_3$$

in which x_5 is altitude of the aircraft (m), x_4 the pitch output (degrees) and x_3 to x_1 are the first to third derivative of pitch.

The measurement equation is given as

$$\begin{aligned} y &= -0.0117x_1 - 0.2519x_2 - 3.006x_3 - 18.64x_4 \\ &\quad - 49.42x_5 + n + d_2 + d_4 \end{aligned}$$

where, n is noise in measurements.

The regulated outputs are altitude x_5 and control signal u, given as

$$z = \begin{bmatrix} x_5 \\ u \end{bmatrix} \tag{26}$$

in which z is the regulated output. In this design, the magnitude of control signal is to be bounded in the regulated outputs to avoid saturation issues. This requirement is also to satisfy the rank condition.

The resulting H_∞ autopilots should have the same number of states as the transfer function of elevon-average-to-altitude obtained in (7). However, since there is a pair of

Table 3 H_∞ autopilot design result

Eigen values	Damping	Frequency
−0.131	1.000	0.131
−0.224	1.000	0.224
−0.439	1.000	0.439
−0.458	1.000	0.458
−2.44 + 8.78*i*	0.268	9.120
−2.44 − 8.78*i*	0.268	9.120
−28.5	1.000	28.50
−83.6	1.000	83.60

doi: 10.1049/iet-cta:20070415

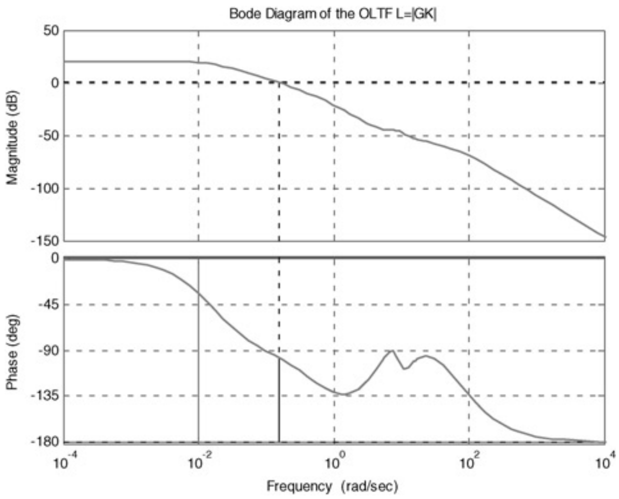

Figure 10 Bode diagram of the compensated open-loop transfer function of H_∞ system

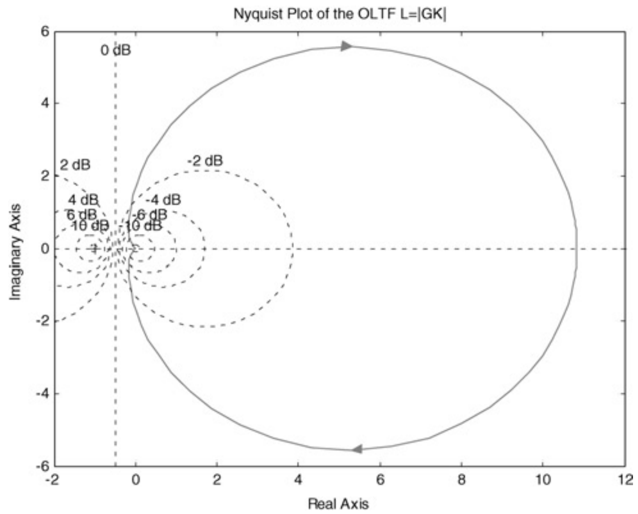

Figure 11 *Nyquist plot of H_∞ system*

common complex conjugate poles and zeroes given by $-2.4446 \pm 8.7786i$ that can cancel each other, the simplified model of H_∞ compensator is given by:

$$K(s) = \frac{-398.51(s + 0.4629)(s + 0.1174)}{(s + 83.62)(s + 28.49)(s + 0.6387)} \quad (27)$$

One pole added at $s = -83.62$ and $s = -28.49$ are to improve high-frequency attenuation. The value of optimal gamma $\gamma\text{-opt} = 8.2611$. Upon several iterations, the resulting estimator gains L and regulators gains K are obtained as follows:

$$L = [0.0010 \quad 0.0001 - 0.00001 - 0.0012 - 0.05769]^{\mathrm{T}} \quad (28)$$

$$K = [7.0138 \quad 38.9153 \quad 606.3590 \quad 389.1771 \quad 56.8942]$$

The resulting closed-loop poles, damping factors and its undamped natural frequency are displayed in Table 3 as follows.

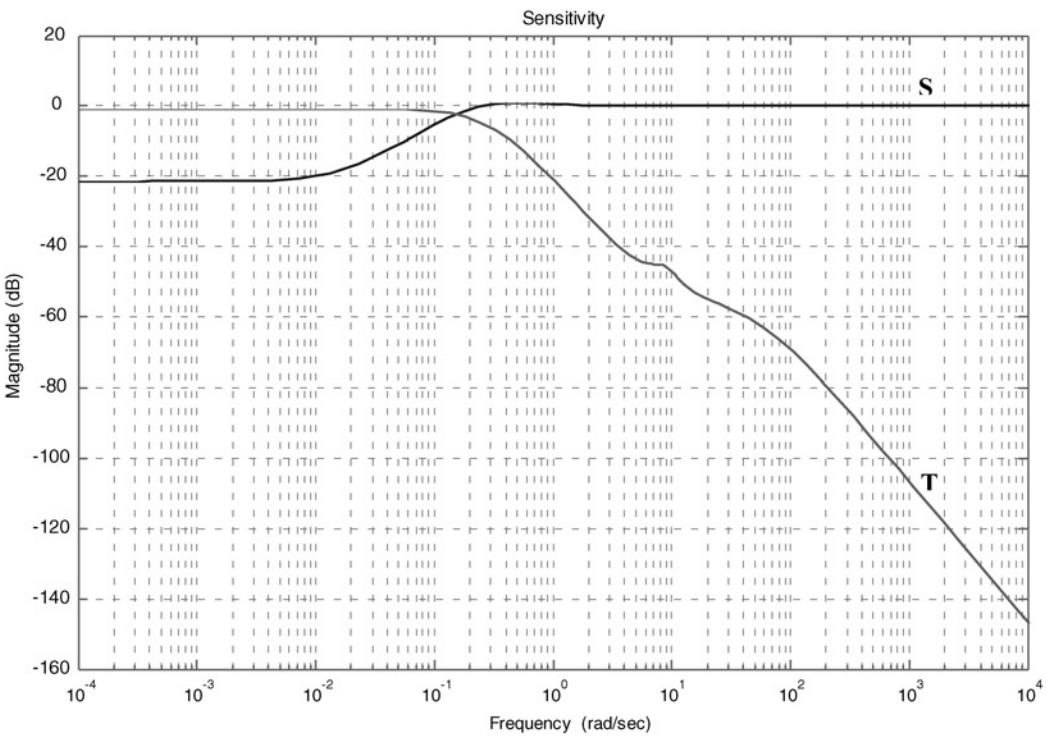

Figure 12 Sensitivity against complementary sensitivity function for H_∞ system

doi: 10.1049/iet-cta:20070415

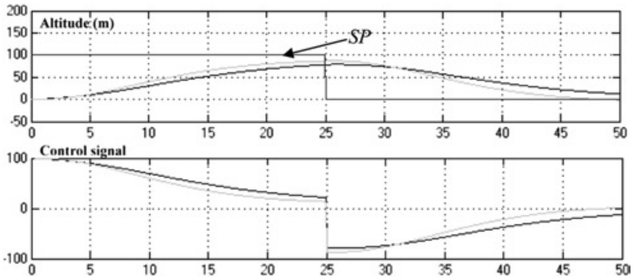

Figure 13 *Taking off, cruising and landing performances (SP denotes its set point), Hinf system is represented by light grey line and H_2 system by dary grey line*

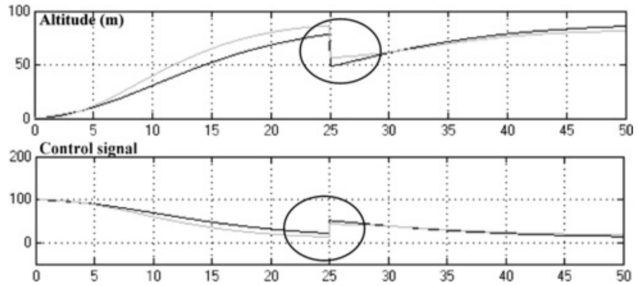

Figure 14 *Closed-loop control systems performances due to 30% disturbances at $t = 25$ s (top), control signal (bottom)*

Hinf system is represented by light grey line, whereas H_2 system is represented by dark grey line

5.3 Frequency response

The resulting compensated open-loop frequency response is given by Fig. 10. It indicates that the resulting GM = Inf and PM = 82.4183°, which is desirable from the point of view of robustness. Moreover, it has the crossover frequency of gain margin $\omega_{cg} = \infty$ (rad/s), and the crossover frequency of phase margin $\omega_{cp} = 0.1548$ (rad/s). Since the Nyquist plot (Fig. 11) does not encircle $-1 + j0$, thus the compensated system is definitely stable. The resulting sensitivity against complementary sensitivity function for our H_∞ system is plotted in Fig. 12.

5.4 Time domain performances

The feasibility of H_∞ frequency domain design is now simulated in time domain. In this scenario, at $t = 0$ s the aircraft was commanded to climb up to 100 m. Subsequently, at $t = 25$ s, the altitude setting point was changed to be zero, see Fig. 13. As can be seen, H_∞ autopilot has successfully achieved better time domain performance (quicker settling time) compared with H_2 counterparts.

Subsequently, in Fig. 14, the effects of disturbances were investigated. An altitude disturbance (30% from the magnitude of setting point), at $t = 25$ s, was injected to the closed-loop control systems to examine how good the closed-loop control systems in overcoming the existing disturbances. It is apparent from Fig. 13 that the disturbance can be overcome with minimum or no overshoots, within reasonable settling time which is desirable from the designer point of view. In aviation world, overshoots are in fact the undesirable transient responses which have to be suppressed. Failure to accomplish this task may create some damages to

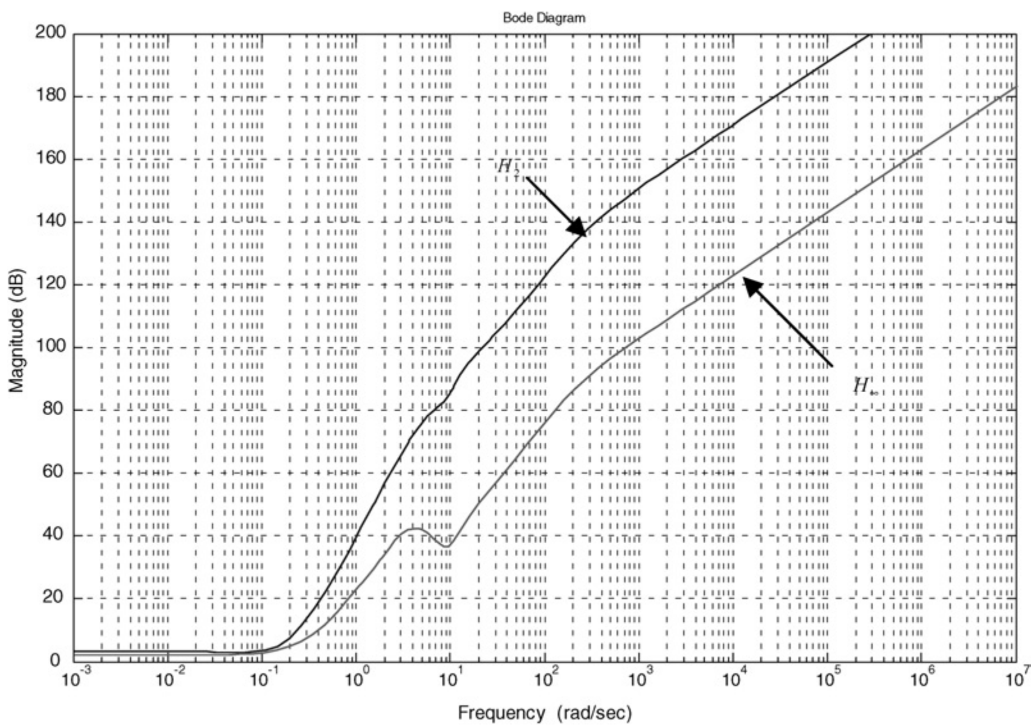

Figure 15 *Maximum tolerable amount of uncertainty, $\Delta = 1/|T(j\omega)|$, for H_2 and $H\infty$ autopilots*

doi: 10.1049/iet-cta:20070415

the whole systems, particularly when the pilot would like to land the aircraft. The oscillations during take off or landing have to be eliminated completely.

6 Maximum tolerable amount of uncertainty $\Delta(j\omega)$

At any given frequency, say for instance, ω_1, the maximum amount of uncertainty, Δ, that can be tolerated while still maintain the stability of the closed loop control system is the reciprocal of the amplitude of the complementary sensitivity function, $|1/|T_o(j\omega)||$, as depicted in Fig. 15. Accordingly, in our design, H_2 autopilot has successfully outperformed H_∞ autopilot in terms of stability robustness due to smaller magnitude of the closed-loop transfer achieved.

7 Concluding remarks

Theoretical developments of robust autopilots using H_∞ and H_2 algorithm have been developed. Our design results indicate the superiority of robust H_∞ autopilot in terms of domain performances compared with H_2 counterpart due to smaller magnitude of the nominal sensitivity function achieved. H_∞ autopilot in fact provides more responsive time domain response as depicted in Fig. 13. Moreover, robust H_∞ autopilot also poses better stability margin (GM = infinity and PM = 82.4183°) compared with its H_2 counterpart (GM = 21.1356 dB, PM = 76.3742°).

Nevertheless, superior time domain performance can be achieved by having smaller magnitude of the nominal sensitivity function, $|S_o|$ at a particular frequency. Accordingly, due to water bed effects, it must be paid by having bigger magnitude of the nominal complementary sensitivity function $|T_o|$. As a result, H_2 autopilot has been superior when it comes to stability robustness compared with its H_∞ counterpart. It turns out that although it is believed that there is no robustness guarantee for H_2 autopilot, it does not necessarily mean that the design result must be lacking or poor of robustness.

We cannot in fact keep both $|S_o|$ and $|T_o|$ small at the same instance. Instead, we can arrange one of them smaller, over one range of frequency, and over the complementary range of frequency another is retained to be smaller. Since the demand of good performance over the design frequency range and the demand of good robustness above this range, in practice, sensitivity is smaller over the design bandwidth $[0, \omega_b]$ and the complementary sensitivity is smaller over the remaining bandwidth, $[\omega_b, \infty]$. At higher frequencies the inaccuracy in modelling is most likely to occur.

8 Acknowledgments

The authors wish to thank Mr Raymond Cooper, the Chief Test Pilot in our group, for his coordination of all test flights and the construction of the P15035 aircraft. The authors also wish to thank the members of the Aerobotics Research Group at Monash University [26].

9 References

[1] LIU M., EGAN G., GE Y.: 'Identification of attitude flight dynamics for an unconventional UAV'. Proc. IEEE/RSJ Int. Conf. Intelligent Robots and Systems, Beijing, China, 9–15 October 2006

[2] SANTOSO F.: 'Robot aircraft dynamics model identification and autopilot designs', Master's thesis Thesis, Electrical and Computer Systems Engineering, Faculty of Engineering, Monash University, 2006

[3] SANTOSO F., LIU M., EGAN G.: 'Optimal control linear quadratic synthesis for an unconventional aircraft'. Proc. 12th Australian Int. Aerospace Congress (AIAC-12), Melbourne, 19–22 March 2007 also as MECSE-5-2007, Department of Electrical & Computer Systems Engineering, Monash University, 2006

[4] BRYSON A.J.R.: 'Control of spacecraft and aircraft' (Princeton University Press, NJ, 1994)

[5] STEVENS L.B., LEWIS F.: 'Aircraft control and simulation' (John Wiley & Sons, 2003, 2nd edn.)

[6] FRANKLIN G., POWELL J.D., WORKMAN M.L., EMAMI-NAENI A.: 'Feedback control of dynamics systems' (Pearson Prentice-Hall, NJ, 2006)

[7] PRATT R.: 'Flight control systems: practical issues in design and implementation' (The Institution of Electrical Engineers, UK, 2000)

[8] GOODWIN G.C., PAYNE R.L.: 'Dynamic system identification: experiment design and data analysis' (Academic Press, Inc London, Ltd, 1977)

[9] SAGE A.P., MELSA J.L.: 'System identification' (Academic Press, Inc, London, Ltd, 1971)

[10] EYKHOFF P.: 'System identification: parameter and state estimation' (John Wiley & Sons, 1974)

[11] MEHRA R.K., LAINIOTIS D.G.: 'System identification advances and case studies' (Academic Press, Inc. London Ltd, 1976)

[12] SAFONOV M.G., LAUB A.J., HARTMANN G.: 'Feedback properties of multivariable systems: the role and use of return difference matrix', *IEEE Trans. Autom. Control*, 1981, **AC-26**, pp. 47–65

[13] DOYLE J.C., GLOVER P., KHARGONEKAR FRANCIS B.: 'State-space solutions to standard H2 and H control problems', *IEEE Trans. Autom. Control*, 1989, **34**, (8), pp. 831–847

[14] GLOVER K., DOYLE J.C.: 'State-space formulae for all stabilizing controllers that satisfy an H norm bound and relations to risk sensitivity', *Syst. Control Lett.*, 1989, **11**, pp. 167–172

[15] ZHOU K., DOYLE J.: 'Essentials of robust control' (Prentice-Hall, 1997)

[16] DOYLE J., FRANCIS B., TANNENBAU A.: 'Feedback control theory' (Mac Milan Publishing Co., 1990)

[17] OGATA K.: 'Modern control engineering' (Prentice-Hall, 2002)

[18] FRANKLIN G.F., POWELL J.D., WORKMAN M.L.: 'Digital control of dynamic systems' (Addison-Wesley, 1990)

[19] SINHA N.K.: 'Linear systems' (John Wiley & Sons, Inc., Canada, 1991)

[20] Micropilot: http://www.micropilot.com, accessed January 2007

[21] Robust control, HIMAT Example http://www.nd.edu/~lemmon/courses/ee555/lecture-14a.pdf, accessed June 2007

[22] KHOSLA P.: 'Real time LQG robotics visual tracking' (Carnegie Mellon University) http://www.cmu.edu/, accessed 27 September 2006)

[23] KULCSAR B.: 'LQG/LTR controller design for an aircraft model', *Period. Polytech.*, 2000, **28**, (1–2), pp. 131–142

[24] AL-SHAMARY N.: 'Robust and gain scheduled flight control systems', Masters thesis, Electrical and Computer Systems Engineering, Faculty of Engineering, Monash University, 2001

[25] SHAHIAN B., HASSUL M.: 'Control systems design using Matlab®' (Prentice-Hall, Englewood Cliffs, NJ, 1993)

[26] Monash Aerobotics: Available at http://www.ctie.monash.edu.au/hargrave/aerobotics.html, 2002, accessed February 2006

IET Control Theory Appl., 2008, Vol. 2, No. 7, pp. 583–594

doi: 10.1049/iet-cta:20070415